

Transport and dynamics of liquid oxygen droplets in supercritical hydrogen streams

By H. MENG¹, G. C. HSIAO¹, V. YANG^{1†} AND J. S. SHUEN²

¹Department of Mechanical Engineering, The Pennsylvania State University,
University Park, PA 16802, USA

²US Department of Energy, Richland Operations Office, Richland,
WA 99352, USA

(Received 18 June 2003 and in revised form 19 October 2004)

The transport and dynamics of an isolated liquid oxygen (LOX) droplet in a supercritical hydrogen stream has been numerically studied based on the complete conservation equations in axisymmetric coordinates. The approach employs a unified treatment of general fluid thermodynamics and transport, and accommodates rapid variations of fluid properties in the transcritical regime. Surface tension of the droplet is ignored in consistency with the supercritical thermodynamic condition. The analysis allows for a systematic investigation into droplet behaviour over broad ranges of fluid thermodynamic states and ambient flow conditions. Detailed flow structures and transport phenomena are examined to reveal various key mechanisms underlying droplet vaporization in a supercritical forced convective environment. In addition, correlations of droplet lifetime and drag coefficient are established in terms of fluid properties, pressure, and free-stream Reynolds number.

1. Introduction

Supercritical droplet vaporization and combustion has long been of serious concern in the development of high-pressure combustion devices, such as diesel, liquid-propellant rocket and gas-turbine engines. The fuel, initially delivered to the combustion chamber at a subcritical temperature, heats up rapidly owing to energy transfer from the ambience and eventually reaches its supercritical state. The process inherently involves an array of intricate phenomena, which conventional droplet theories developed for low-pressure conditions cannot handle properly (Bellan 2000; Yang 2000).

Most previous studies of supercritical droplet vaporization (Hsieh, Shuen & Yang 1991; Shuen, Yang & Hsiao 1992; Delplanque & Sirignano 1993; Yang, Lin & Shuen 1994; Lafon 1995; Harstad & Bellan 1998) focused on droplet behaviour at quiescent conditions. Effects of free-stream velocity on droplet vaporization and dynamics in forced-convective environments have not been addressed in detail. Daou & Rogg (1998) numerically studied fuel droplet combustion in supercritical convective environments. The droplet was assumed to reach its supercritical state immediately upon being injected into the combustion chamber. The fluid volumetric properties were further assumed to obey the ideal gas law, with all the other thermophysical properties treated as constants. The approach ignored many salient features of

† Author to whom correspondence should be addressed: vigor@psu.edu

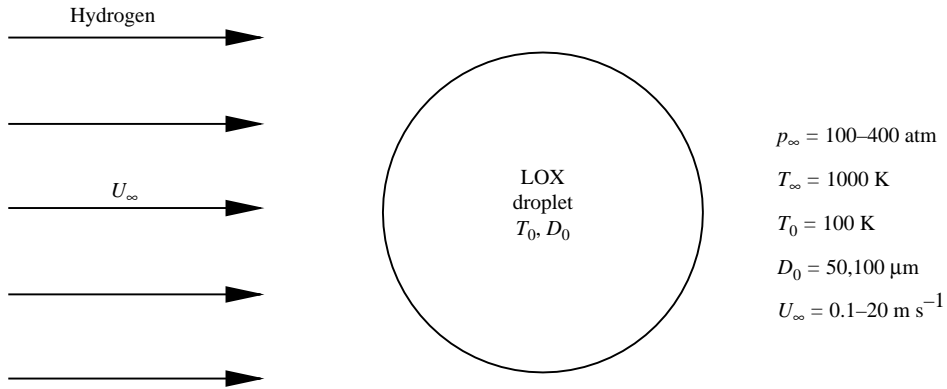


FIGURE 1. Schematic diagram of droplet vaporization in forced convective environment.

supercritical droplet vaporization, such as thermodynamic non-idealities and transport anomalies during the transition from a subcritical to a supercritical state.

The present work attempts to conduct a comprehensive investigation into liquid oxygen (LOX) droplet vaporization in supercritical hydrogen streams over a broad range of pressure (100–400 atm) and Reynolds number (2.5–300). The approach is based on a unified treatment of general fluid thermodynamics and a robust preconditioning numerical scheme (Meng & Yang 2003). Rapid variations of fluid properties in the transcritical regime are accommodated, whereas the surface tension of the droplet is neglected in consistency with the supercritical thermodynamic condition. Various fundamental issues associated with droplet dynamics and related transport phenomena at high pressures are examined systematically, with emphasis placed on the distinct characteristics of cryogenic fluids. Correlations of the mass and momentum transfer between droplet and free stream are established in terms of droplet thermodynamic state and ambient flow conditions. The results can be used effectively as a physical submodel for high-pressure spray combustion analyses.

2. Theoretical formulation

The physical model of interest includes an isolated LOX droplet vaporizing in a supercritical hydrogen stream, as shown in figure 1. The initial droplet temperature is uniformly distributed at a subcritical value, but the pressure and temperature of the ambient hydrogen are in the supercritical regime of oxygen. Once the droplet is injected into the flow, its surface heats up and soon reaches the thermodynamic critical mixing state owing to the cryogenic fluid properties of oxygen and rapid energy transfer. For example, if the initial temperature of the droplet is 100 K and the ambient pressure is 100 atm, the droplet surface may reach the critical mixing state in a short time span with less than 5% of the mass evaporated (Yang *et al.* 1994; Lafon 1995). The process becomes even faster with increasing ambient pressures. Table 1 shows the effects of pressure on the critical mixing properties for the binary O_2/H_2 system (Yang *et al.* 1994). The critical mixing temperature is lower than the critical temperature of pure oxygen (i.e. 154.6 K), and decreases with increasing pressure. The mass fraction of hydrogen at the critical mixing state, however, increases with increasing pressure.

Prior to the occurrence of thermodynamic criticality, the droplet surface conditions can be determined by the conservation of mass and energy across the surface along

Pressure (atm)	Critical mixing temperature (K)	Critical mixing composition of O ₂
100	142.8	0.735
200	127.2	0.561
400	116.0	0.496

 TABLE 1. Critical mixing properties of O₂/H₂ system.

with the assumption of thermodynamic phase equilibrium. Once the critical mixing state is reached at the surface, the enthalpy of vaporization and surface tension vanish. The entire flow field (including both the oxygen droplet and surrounding hydrogen) becomes essentially a continuous medium, and no well-defined liquid/gas interfacial boundary exists, as for a subcritical droplet. The droplet interior, however, still remains at the liquid state with a subcritical temperature distribution. The subsequent droplet evolution is diffusion controlled, and the effect of interphase thermodynamics disappears. Since thermal penetration proceeds at a rate faster than mass diffusion at supercritical conditions, the critical mixing temperature and composition cannot be sustained at the same location, as discussed in detail in §5.1. The droplet can be conveniently defined as the dense fluid pocket enclosed with the surface that attains the critical mixing temperature. It should be emphasized that the supercritical droplet is different from its subcritical counterpart in that the surface tension and enthalpy of vaporization vanish at the droplet surface.

Owing to the cryogenic fluid properties of oxygen, the droplet reaches its thermodynamic critical mixing state almost instantaneously upon introduction into the hydrogen flow under most practical conditions. A single-phase supercritical fluid model is therefore used herein to facilitate numerical analysis. The flow field is assumed to be laminar and axisymmetric owing to the low-Reynolds-number conditions of concern. If body forces and thermal radiation are ignored, the conservation laws of mass, momentum, energy and species concentration can be written in the following vector form:

$$\frac{\partial \mathbf{Q}}{\partial t} + \frac{\partial(\mathbf{E} - \mathbf{E}_v)}{\partial x} + \frac{\partial(\mathbf{F} - \mathbf{F}_v)}{\partial r} = S, \quad (2.1)$$

where x and r represent the axial and radial coordinates, respectively. The independent variable vector \mathbf{Q} is defined as

$$\mathbf{Q} = r[\rho \quad \rho u_x \quad \rho u_r \quad \rho e_t \quad \rho Y_i]^T, \quad (2.2)$$

where superscript T denotes the transpose of the vector. Standard notation in fluid mechanics is used here, with ρ , (u_x, u_r) , e_t and Y_i being the density, velocity components, specific total energy and mass fraction of species i , respectively. The convective-flux vectors, \mathbf{E} and \mathbf{F} , in the axial and radial directions, respectively, take the forms

$$\mathbf{E} = r[\rho u_x \quad \rho u_x^2 + p \quad \rho u_x u_r \quad (\rho e_t + p)u_x \quad \rho u_x Y_i]^T, \quad (2.3)$$

$$\mathbf{F} = r[\rho u_r \quad \rho u_x u_r \quad \rho u_r^2 + p \quad (\rho e_t + p)u_r \quad \rho u_r Y_i]^T. \quad (2.4)$$

The corresponding diffusion-flux vectors are

$$\mathbf{E}_v = r[0 \quad \tau_{xx} \quad \tau_{xr} \quad u_x \tau_{xx} + u_r \tau_{xr} - q_x \quad -\rho \hat{u}_i Y_i]^T, \quad (2.5)$$

$$\mathbf{F}_v = r[0 \quad \tau_{xr} \quad \tau_{rr} \quad u_x \tau_{xr} + u_r \tau_{rr} - q_r \quad -\rho \hat{v}_i Y_i]^T, \quad (2.6)$$

where \hat{u}_i and \hat{v}_i are the mass diffusion velocities of species i in the axial and radial directions, respectively. In the above equations, the normal and shear stresses are given as

$$\tau_{xx} = \mu \left(\frac{4}{3} \frac{\partial u_x}{\partial x} - \frac{2}{3} \frac{\partial u_r}{\partial r} \right), \quad (2.7a)$$

$$\tau_{rr} = \mu \left(\frac{4}{3} \frac{\partial u_r}{\partial r} - \frac{2}{3} \frac{\partial u_x}{\partial x} \right), \quad (2.7b)$$

$$\tau_{xr} = \mu \left(\frac{\partial u_r}{\partial x} + \frac{\partial u_x}{\partial r} \right), \quad (2.7c)$$

where μ represents the dynamic viscosity. For convenience in the numerical treatment, the viscous terms are re-organized, and those terms related to axisymmetric geometry are considered as source terms, as presented in (2.13). The effect of the second (i.e. bulk) viscosity is ignored in the above formulation owing to the lack of reliable data within the range of fluid thermodynamic states of concern. It is worth noting that the stress terms associated with the second viscosity probably become significant for a supercritical fluid in which volume dilation plays an important role in dictating the flow evolution. This issue remains to be further investigated.

The thermal diffusion terms contain contributions from heat conduction and mass diffusion.

$$q_x = -\lambda \frac{\partial T}{\partial x} + \rho \sum_{i=1}^N \bar{h}_i Y_i \hat{u}_i, \quad q_r = -\lambda \frac{\partial T}{\partial r} + \rho \sum_{i=1}^N \bar{h}_i Y_i \hat{v}_i, \quad (2.8)$$

where T is the temperature, λ the thermal conductivity, and \bar{h}_i the partial-mass enthalpy of species i . For a general fluid mixture at a specified state, the properties of each constituent component, such as the specific enthalpy in (2.8), should be defined based on the concept of partial properties. According to classical thermodynamic theories, a partial-mass property is defined as

$$\bar{\phi}_i = \left(\frac{\partial m \phi}{\partial m_i} \right)_{T, p, m_{j \neq i}}, \quad (2.9)$$

where m is the total mass of the mixture and ϕ the specific property per unit mass of a fluid mixture (Meng & Yang 2003). The indices, i and j , range from 1 to N . To facilitate numerical treatment, a partial-density property is also defined

$$\tilde{\phi}_i = \left(\frac{\partial \rho \phi}{\partial \rho_i} \right)_{T, \rho_{j \neq i}}. \quad (2.10)$$

The partial-mass and partial-density enthalpy of species i can thus be expressed as

$$\bar{h}_i = \left(\frac{\partial m h}{\partial m_i} \right)_{T, p, m_{j \neq i}}, \quad (2.11a)$$

$$\tilde{h}_i = \left(\frac{\partial \rho h}{\partial \rho_i} \right)_{T, \rho_{j \neq i}}. \quad (2.11b)$$

The mass diffusion velocities consist of contributions from both concentration (i.e. Fick's law) and temperature (i.e. Soret effect) gradients.

$$Y_i \hat{u}_i = -D_{im} \frac{\partial Y_i}{\partial x} - \frac{D_i^T}{\rho T} \frac{\partial T}{\partial x}, \quad Y_i \hat{v}_i = -D_{im} \frac{\partial Y_i}{\partial r} - \frac{D_i^T}{\rho T} \frac{\partial T}{\partial r}, \quad (2.12)$$

where D_{im} is the effective mass diffusion coefficient of species i , and D_i^T is the multi-component thermal diffusion coefficient.

The source term in (2.1), S , arises from axisymmetric geometry and can be written as

$$S = \begin{bmatrix} 0 \\ -\frac{\partial}{\partial x} \left(\frac{2}{3} \mu u_r \right) \\ p - \frac{4}{3} \frac{\mu u_r}{r} + \frac{2}{3} \mu \frac{\partial u_x}{\partial x} - \frac{2}{3} u_r \frac{\partial \mu}{\partial r} \\ -\frac{\partial}{\partial x} \left(\frac{2}{3} \mu u_x u_r \right) - \frac{\partial}{\partial r} \left(\frac{2}{3} \mu u_r^2 \right) \\ 0 \end{bmatrix}. \quad (2.13)$$

3. Property evaluation

3.1. Thermodynamic properties

One major challenge in the analysis of supercritical droplet behaviour is the establishment of a unified property evaluation scheme capable of treating thermodynamic properties of pure substances and mixtures over the entire fluid thermodynamic states from compressed liquid to dilute gas. At high pressures, models normally used to represent ideal-gas behaviour may encounter significant difficulties. From the microscopic point of view, the intermolecular mean free paths tend to decrease with increasing pressure, and consequently the molecular volume and intermolecular forces are no longer negligible as in the case for idealized fluids. For convenience, each property can be expressed as the sum of an ideal-gas property at the same temperature and a thermodynamic departure function, which takes into account the dense-fluid correction (Yang 2000). For example, the specific internal energy of a general fluid mixture can be expressed as

$$e(T, \rho) = e_0(T) + \int_{\rho_0}^{\rho} \left[\frac{p}{\rho^2} - \frac{T}{\rho^2} \left(\frac{\partial p}{\partial T} \right)_{\rho} \right] d\rho, \quad (3.1)$$

where subscript 0 represents a reference thermodynamic state in the limit of an ideal gas.

The general approach outlined above can be applied to any equation of state. In the current study, a modified Soave–Redlich–Kwong (SRK) equation of state is used to represent the fluid p-V-T behaviour because of its validity over a broad range of thermodynamic states (Graboski & Daubert 1978*a, b*, 1979). The SRK equation of state takes the form

$$p = \frac{\rho R_u T}{(Mw - b\rho)} - \frac{a\alpha}{Mw} \frac{\rho^2}{(Mw + b\rho)}, \quad (3.2)$$

where R_u is the universal gas constant and Mw the molecular weight of a fluid mixture. The two parameters, a and b , account for the effects of attractive and

repulsive forces among molecules, respectively. The third parameter, α , is a function of temperature.

Based on the SRK equation of state, the specific internal energy of a general fluid mixture is derived as

$$e(T, \rho) = e_0(T) + \frac{T^2}{bMw} \left(\frac{\partial a\alpha/T}{\partial T} \right)_{\rho, Y_i} \ln \left(\frac{Mw + b\rho}{Mw + b\rho_0} \right). \quad (3.3)$$

Substituting (3.3) into (2.10) yields the partial-density internal energy of species i

$$\begin{aligned} \tilde{e}_i = e_{i,0} + \frac{2}{bMw_i} \left[\sum_j^N X_j \left(T \frac{\partial}{\partial T} (a_{ij}\alpha_{ij}) - a_{ij}\alpha_{ij} \right) \right] \ln \left(\frac{Mw + b\rho}{Mw + b\rho_0} \right) \\ + \frac{b_i}{bMw_i} \left[T \frac{\partial}{\partial T} (a\alpha) - a\alpha \right] \left[\frac{\rho}{Mw + b\rho} - \frac{1}{b} \ln \left(\frac{Mw + b\rho}{Mw + b\rho_0} \right) \right], \end{aligned} \quad (3.4)$$

where N is the number of species in the mixture and X_i is the mole fraction of species i . A relationship for the partial-mass enthalpy, \bar{h}_i , exists

$$\bar{h}_i = \tilde{e}_i + \left(\frac{\partial p}{\partial \rho_i} \right)_{T, \rho_{j \neq i}} \left[1 - \rho \left(\frac{\partial h}{\partial p} \right)_{T, Y_j} \right]. \quad (3.5)$$

The constant-volume heat capacity is derived as

$$C_v = C_{v,0} + \frac{T}{bMw} \frac{\partial^2}{\partial T^2} (a\alpha) \ln \left(\frac{Mw + b\rho}{Mw + b\rho_0} \right). \quad (3.6)$$

Details of the above derivations and the related partial derivatives can be found in Meng & Yang (2003).

3.2. Transport properties

Accurate evaluation of transport properties is crucial for the study of supercritical fluid behaviour. The extended corresponding-state (ECS) principle of Ely & Hanley (1981, 1983) is used herein to estimate the viscosity and thermal conductivity of a mixture over its entire fluid thermodynamic state. The basic idea of the ECS principle is to assume that the properties of a single-phase fluid can be evaluated via conformal mappings of temperature and density to those of a given reference fluid. For a multicomponent system, accounting for changes in properties due to mixing is much more complicated. A pseudo pure-substance model is adopted to evaluate the properties of a mixture, treating the mixture as a single-phase pure substance with its own set of properties evaluated via the ECS principle. This method improves prediction accuracy and requires only limited data (i.e. critical properties and Pitzer's accentric factor) for each constituent component. According to the corresponding-state principle, a transport property of a fluid mixture can be expressed as

$$\eta_x(T, \rho) = \eta_0(T_0, \rho_0) F_\eta, \quad (3.7)$$

where subscript x refers to the fluid of interest, and 0 to the reference fluid. The parameter F_η represents the mapping function.

Viscosity

Estimation of the viscosity of a fluid mixture can be made by means of the corresponding-state method described in the preceding section.

$$\mu_x(T, \rho) = \mu_0(T_0, \rho_0) F_\mu \chi_\mu. \quad (3.8)$$

The quantity χ_μ is a correction factor accounting for the effect of non-correspondence. Its magnitude is always close to unity, based on the modified Enskog theory (Ely 1981). In the present work, methane is chosen as the reference fluid because of the availability of reliable data correlated over a wide range of experimental conditions. The result shows excellent agreement over the entire fluid state, from compressed liquid to dilute gas.

It is generally accepted that viscosity and thermal conductivity can be divided into three contributions and correlated in terms of density and temperature (Vesovic & Wakeham 1991). For instance, the viscosity of the reference fluid can be written as

$$\mu_0(\rho_0, T_0) = \mu_0^0(T_0) + \Delta\mu_0^{exc}(\rho_0, T_0) + \Delta\mu_0^{crit}(\rho_0, T_0). \quad (3.9)$$

The first term on the right-hand side represents the value in the dilute-gas limit, which is independent of density and can be accurately predicted by kinetic theories (Ely & Hanley 1981, 1983). The second term is the excess viscosity which, with the exclusion of unusual variations near the critical point, characterizes the deviation from μ_0 for a dense fluid. The third term refers to the critical enhancement which accounts for the anomalous increase above the background viscosity (i.e. the sum of μ_0^0 and $\Delta\mu_0^{exc}$) as the critical point is approached. The theory of non-classical critical behaviour predicts that, in general, properties that diverge strongly in pure fluids near the critical points will diverge only weakly in mixtures because of the different physical criteria for criticality in a pure fluid and a mixture (Levelt Sengers 1991). Because the effect of critical enhancement is not well-defined for a mixture and is likely to be small, the third term $\Delta\mu_0^{crit}$ is not considered in the existing analyses of supercritical droplet vaporization.

Thermal conductivity

Evaluation of thermal conductivity must be conducted carefully for two reasons. First, the one-fluid model must ignore the contribution of diffusion to thermal conductivity. Secondly, the effect of internal degrees of freedom on thermal conductivity cannot be correctly taken into account by the corresponding-state argument. As a result, thermal conductivity of a pure substance or mixture is generally divided into two contributions (Ely & Hanley 1983),

$$\lambda_x(\rho, T) = \lambda'_x(T, \rho) + \lambda''_x(T). \quad (3.10)$$

The former, $\lambda'_x(T, \rho)$, arises from molecular collision or translation, while the latter, $\lambda''_x(T)$, is due to the effects of energy transfer via the internal degrees of freedom. The collision/translation contribution is evaluated using the extended corresponding-state method,

$$\lambda'_x(T, \rho) = \lambda'_0(T_0, \rho_0)F_\lambda\chi_\lambda, \quad (3.11)$$

where F_λ is the scaling factor identical to that used in (3.8) for mixture viscosity. A small correction factor χ_λ is used to compensate the non-correspondence behaviour, and can be estimated using the modified Enskog theory and fluid p-V-T properties. The quantity of a reference fluid, $\lambda'_0(T_0, \rho_0)$, can be further divided into three parts:

$$\lambda'_0(\rho_0, T_0) = \lambda_0^*(T) + \Delta\lambda_0^{exc}(\rho_0, T_0) + \Delta\lambda_0^{crit}(\rho_0, T_0), \quad (3.12)$$

where $\lambda_0^*(T)$ is the value in the dilute-gas limit, $\Delta\lambda_0^{exc}$ the excess thermal conductivity, and $\Delta\lambda_0^{crit}$ the critical enhancement. Since the effect of the anomalous variation of thermal conductivity appears to be small for a mixture near its critical locus, the critical enhancement, $\Delta\lambda_0^{crit}$, is not accounted for in the present work.

The contribution of internal degrees of freedom, $\lambda''_x(T)$, can be evaluated via a semi-empirical mixing rule

$$\lambda''_x(T) = \sum_i^N \sum_j^N X_i X_j \lambda''_{ij}(T), \quad (3.13)$$

where $\lambda''_{ij}(T)$ is a binary thermal conductivity defined as

$$(\lambda''_{ij})^{-1} = 2[(\lambda''_i)^{-1} + (\lambda''_j)^{-1}]. \quad (3.14)$$

The internal contribution of component i is calculated by the modified Eucken correlation (Ely & Hanley 1983) for polyatomic gases as

$$\frac{\lambda''_i M w_i}{\mu_i^g} = 1.32(C_{p,i}^g - \frac{5}{2}R_u), \quad (3.15)$$

where the properties μ_i^g and $C_{p,i}^g$ are the dilute-gas viscosity and ideal-gas heat capacity of component i , respectively, and R_u the universal gas constant.

Mass diffusivity

Estimation of the binary mass diffusivity for a fluid mixture at high density represents a more challenging task than evaluating the other transport properties, owing to the lack of a formal theory or even a theoretically based correlation. Takahashi (1974) has suggested a simple scheme for predicting the binary mass diffusivity of a dense fluid by means of a corresponding-state approach. This scheme appears to be the most complete to date, and has demonstrated moderate success in the limited number of tests conducted. The approach proceeds in two steps. First, the binary mass diffusivity of a dilute gas is determined using an empirical correlation, such as that of Fuller (Reid, Prausnitz & Poling 1987).

$$D_{ij} = \frac{0.00143T^{1.75}}{pMw_{ij}^{1/2}[(\Sigma_v)_i^{1/3} + (\Sigma_v)_j^{1/3}]^2}, \quad (3.16)$$

where D_{ij} is the binary mass diffusivity, Mw_{ij} the combined molecular weight, and Σ_v the summation of atomic diffusion volumes, as tabulated in Reid *et al.* (1987, table 11-1). The calculated data are then corrected in accordance with a generalized chart in terms of reduced temperature and pressure.

$$\frac{D_{ij}p}{(D_{ij}p)^+} = f(T_r, p_r), \quad (3.17)$$

where superscript + indicates the low-density value as given in (3.16). The function $f(T_r, p_r)$ represents a scaling factor of pressure, which is tabulated by Takahashi and also shown in Reid *et al.* (1987, figure 11-3).

Table 2 lists the thermophysical properties of a binary mixture comprising of 50% of hydrogen and 50% of oxygen at three different pressures of 1, 100 and 400 atm. The effects of pressure on fluid properties are clearly demonstrated.

4. Numerical algorithm

Droplet vaporization and combustion typically involve fluid motions in a velocity range from molecular diffusion to low subsonic speed. Contemporary numerical algorithms developed for compressible flows are often ineffective at such low-velocity

	1 atm	100 atm	400 atm
Density (kg m^{-3})	1.03×10^0	1.04×10^2	3.26×10^2
Heat capacity ($\text{J kg}^{-1} \text{K}^{-1}$)	1.68×10^3	2.01×10^3	2.27×10^3
Thermal conductivity ($\text{W m}^{-1} \text{K}^{-1}$)	3.88×10^{-2}	5.38×10^{-2}	9.76×10^{-2}
Viscosity (N s m^{-2})	1.34×10^{-5}	1.49×10^{-5}	2.25×10^{-5}
Mass diffusivity ($\text{m}^2 \text{s}^{-1}$)	4.04×10^{-5}	3.88×10^{-7}	9.92×10^{-8}
Prandtl number	5.81×10^{-1}	5.55×10^{-1}	5.23×10^{-1}
Schmidt number	3.20×10^{-1}	3.70×10^{-1}	6.96×10^{-1}
Lewis number	5.51×10^{-1}	6.67×10^{-1}	1.33×10^{-0}

TABLE 2. Effects of pressure on thermophysical properties of hydrogen/oxygen mixture (50% of H_2 and 50% of O_2 in molar fraction) at 200 K.

conditions. There are two well-recognized reasons for this difficulty (Choi & Merkle 1993). First, the eigenvalues of the system become disparate at low flow velocities, thereby adversely affecting the convergence characteristics of numerical solutions. Secondly, the pressure terms in the momentum equations become singular as the Mach number approaches zero and consequently result in a large round-off error. In order to circumvent the above computational difficulties, a preconditioning scheme along with a dual time-stepping integration method (Shuen, Chen & Choi 1993; Hsieh & Yang 1997) has been developed. The scheme is established in two steps. First, rescaled pressure terms are used in the momentum equations to minimize round-off errors at low Mach numbers. The second step incorporates a set of well-conditioned artificial terms into the conservation laws to enhance numerical efficiency and stability. An iterative procedure is then followed to achieve a converged solution in the pseudo-time domain, which corresponds to a temporal-accurate solution in the physical-time domain. The resulting governing equations are written as

$$\Gamma \frac{\partial \hat{\mathbf{Q}}}{\partial \tau} + \frac{\partial \mathbf{Q}}{\partial t} + \frac{\partial(\mathbf{E} - \mathbf{E}_v)}{\partial x} + \frac{\partial(\mathbf{F} - \mathbf{F}_v)}{\partial r} = \mathbf{S}, \quad (4.1)$$

where τ represents the pseudo time and Γ is the preconditioning matrix. The pseudo-time variable vector $\hat{\mathbf{Q}}$ is defined as

$$\hat{\mathbf{Q}} = r[p_g \quad u_x \quad u_r \quad h \quad Y_i]^T, \quad (4.2)$$

where p_g is the gauge pressure resulting from pressure decomposition.

One major advantage of the dual time-stepping integration method is that the convergence of the iterative process is determined by the rescaled eigenvalues in the pseudo-time domain, not by the original eigenvalues, which become disparate at low flow velocity. This feature allows flexibility in selecting the time steps in both the pseudo- and physical-time frames. The physical-time step is determined based on the characteristic evolution of the unsteady flow under consideration, while the pseudo-time step depends on the numerical stability of the algorithm and can be adjusted to obtain optimum convergence.

The preconditioning scheme is further equipped with the unified treatment of general fluid thermodynamics outlined in the preceding sections. The analysis is based on the concepts of partial-mass and partial-density properties, as defined in (2.9) and (2.10). All of the thermodynamic properties and numerical Jacobian matrices are derived directly from fundamental thermodynamics theories, rendering a robust

algorithm valid for fluid flows at all speeds and at all thermodynamic states. Details of the overall numerical algorithm are given in Meng & Yang (2003).

5. Results and discussions

The theoretical model and numerical scheme described in the preceding sections have been validated against several test problems involving vaporization of *n*-heptane droplets in high-pressure quiescent nitrogen gas environments (Meng & Yang 2003) and supercritical fluid jet dynamics (Zong *et al.* 2004). After validation, the analysis was applied to study the vaporization characteristics of liquid oxygen (LOX) droplets in supercritical hydrogen streams. At $t = 0$ ms, a droplet is suddenly released in the hydrogen stream, as shown in figure 1. The ambient hydrogen temperature was taken to be 1000 K. The initial droplet temperature of 100 K corresponds to the LOX injection temperature in many operational rocket engines, such as the Space Shuttle main engines and the Vulcain engines used in the Ariane 5 launch vehicles. In order to examine the effects of ambient flow conditions on droplet behaviour and associated transport phenomena, a parametric study covering a wide range of pressure (100–400 atm) and velocity (0.1–20 m s⁻¹) was conducted. The present numerical investigation focuses on axisymmetric flow conditions, with the corresponding free-stream Reynolds numbers based on the initial droplet diameter ($Re = U_\infty D_0 / \nu_\infty$) less than 300. The present analysis is intended to explore the fundamental physics of supercritical droplet transport and dynamics.

Within the pressure range of the current interest, the droplet initial temperature is slightly lower than the critical mixing temperature of the oxygen/hydrogen binary mixture (e.g. $T_c = 142.79$ K at $p = 100$ atm). Thermodynamic criticality is reached at the droplet surface almost instantaneously upon introduction of the droplet into the hydrogen stream with less than 5% of the oxygen mass evaporated, owing to rapid heat transfer from the ambient flow (Yang *et al.* 1994; Lafon 1995). Once this occurs, the liquid and gas phases coexist on the droplet surface at the critical mixing state. The enthalpy of vaporization and surface tension reduce to zero, and the mixture properties as well as their spatial gradients vary continuously across the surface. The droplet interior, however, still remains at the liquid state with a subcritical temperature distribution. The subsequent vaporization process becomes diffusion/convection controlled, and the effect of interfacial thermodynamics disappears.

5.1. Effects of ambient pressure and velocity on droplet and flow evolution

Calculations were first carried out for the initial droplet diameter of 100 μ m under various flow conditions. Figure 2 shows six frames of isotherms and isopleths of oxygen concentration at a convective velocity of 2.5 m s⁻¹ and an ambient pressure of 100 atm. The free-stream Reynolds number Re is 31, based on the initial droplet diameter. Soon after the introduction of the droplet into the hydrogen stream, the flow adjusts to form a boundary layer near the surface. The vaporized oxygen cannot accumulate on the front surface of the droplet, and is carried downstream through convection and mass diffusion. The evolution of the temperature field exhibits features distinct from that of the concentration field owing to the disparate time scales associated with thermal and mass diffusion processes (i.e. the Lewis number $Le \neq 1$, where $Le = \lambda / \rho C_p D_{im}$). The thermal wave penetrates into the droplet interior faster than the surrounding hydrogen species does. Since the liquid core possesses large momentum inertia and moves more slowly than the vaporized oxygen, at $t = 0.79$ ms, the droplet (delineated by the dark region in the temperature contours) reveals an

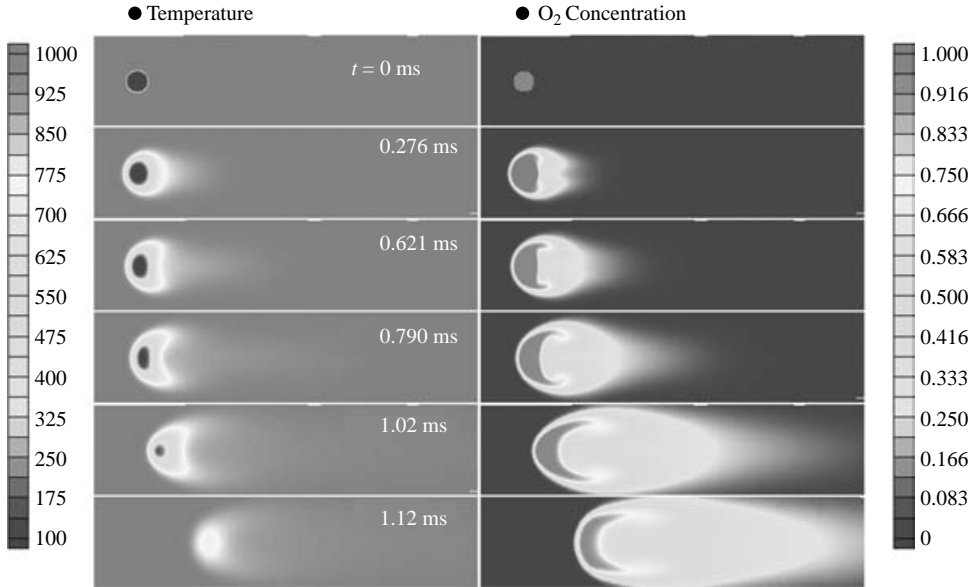


FIGURE 2. LOX droplet vaporization in supercritical hydrogen flow; $p = 100$ atm, $U_\infty = 2.5 \text{ m s}^{-1}$, $D_0 = 100 \mu\text{m}$.

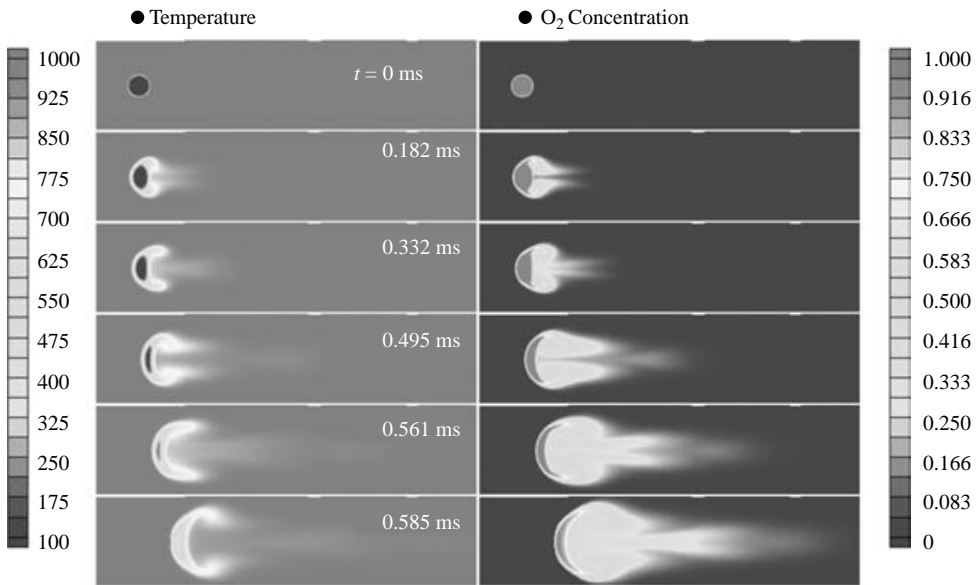


FIGURE 3. LOX droplet vaporization in supercritical hydrogen flow; $p = 400$ atm, $U_\infty = 2.5 \text{ m s}^{-1}$, $D_0 = 100 \mu\text{m}$.

olive shape while the oxygen concentration contours deform into a crescent shape with the edge bent to the streamwise direction. At $t = 1.08$ ms, the subcritical liquid core disappears, leaving behind a puff of dense oxygen fluid which is convected further downstream with increasing velocity until it reaches the momentum equilibrium with the ambient hydrogen flow.

Figure 3 presents droplet evolution at an ambient pressure of 400 atm. The free-stream velocity remains at 2.5 m s^{-1} . The effect of pressure on droplet dynamics

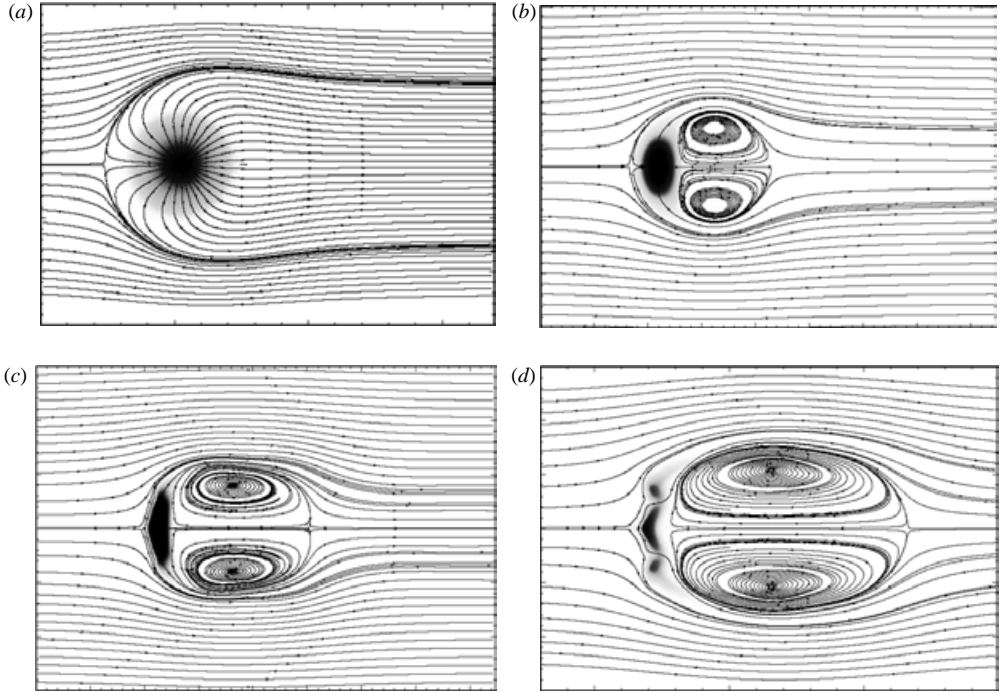


FIGURE 4. LOX droplet vaporization in supercritical hydrogen flow for $p = 100$ atm and $D_0 = 100 \mu\text{m}$: (a) spherical mode; $U_\infty = 0.2 \text{ m s}^{-1}$, $t = 0.61 \text{ ms}$; (b) deformation mode; $U_\infty = 1.5 \text{ m s}^{-1}$, $t = 0.61 \text{ ms}$; (c) stripping mode; $U_\infty = 5 \text{ m s}^{-1}$, $t = 0.17 \text{ ms}$; (d) penetration mode; $U_\infty = 15 \text{ m s}^{-1}$, $t = 0.17 \text{ ms}$.

can be determined by direct comparison with figure 2. Several distinct phenomena are observed. First, the droplet deformation is enhanced with increasing ambient pressure. Here, the Reynolds number is 3.75 times larger than that at 100 atm. The hydrogen stream carries higher momentum and exerts stronger force on the droplet, and, as such, promotes its deformation. Secondly, the droplet lifetime decreases with increasing ambient pressure because the higher convective momentum increases the contact surface exposed to the hot stream, thereby facilitating the transfer of thermal energy to the droplet. Thirdly, the increased ambient pressure enhances the gradients of temperature and oxygen concentration. Although the blowing effect due to droplet vaporization is stronger at high pressure, the large momentum transfer reduces the convective residence time and forms a thinner boundary layer near the surface.

Figure 4 summarizes the streamline patterns and oxygen concentration contours of the four different modes commonly observed in supercritical droplet vaporization. The droplet may remain in a spherical configuration, deform to an olive shape, or even be shattered into fragments, depending on the local flow conditions. Unlike low-pressure cases, in which the large shear stress at the gas–liquid interface induces internal flow circulation in the liquid core (Prakash & Sirignano 1978, 1980), no discernible recirculation takes place in the droplet interior, regardless of the Reynolds number and deformation mode. This may be attributed to the vanished surface tension at supercritical conditions. In addition, the droplet regresses so fast that a fluid element in the interfacial region may not acquire the time sufficient for establishing an internal vortical flow before it vaporizes. The rapid deformation of the droplet configuration

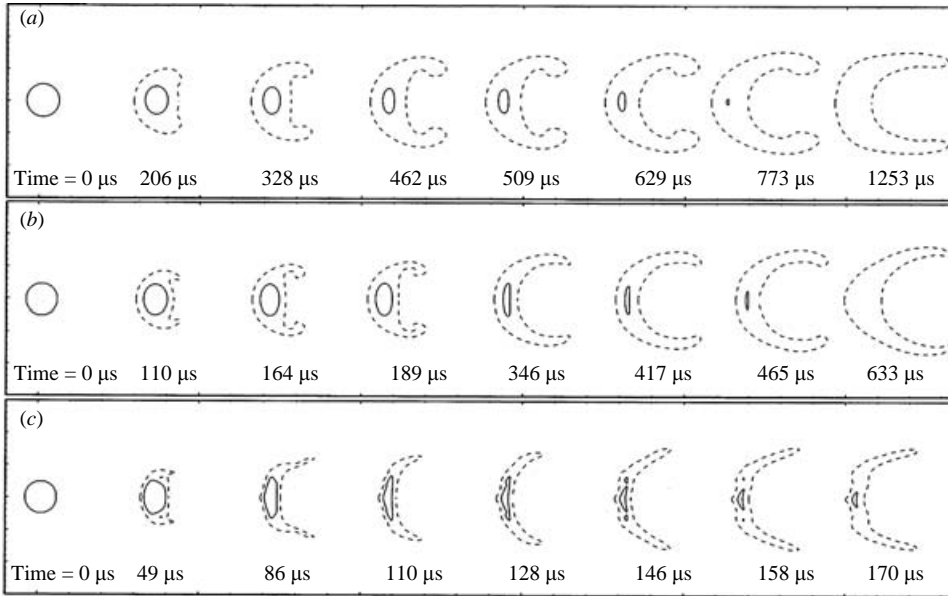


FIGURE 5. Effect of ambient velocity on evolution of droplet critical surfaces, LOX/H₂ system with $p = 100 \text{ atm}$ and $D_0 = 100 \mu\text{m}$. (a) $U_\infty = 2.5 \text{ m s}^{-1}$, (b) 5 m s^{-1} , (c) 15 m s^{-1} . —, critical mixing temperature; ---, critical mixing composition.

further precludes the generation of stationary shear stress in the liquid core and consequently restricts the development of a recirculation pattern.

The spherical mode shown in figure 4(a) typically occurs at very low Reynolds numbers. Although flow separation is encouraged by LOX vaporization, no recirculating eddy is found in the wake behind the droplet. The vorticity generated is too weak to form any confined eddy. When the ambient velocity increases to 1.5 m s^{-1} , the droplet deforms into an olive shape with a recirculating ring attached behind it, as shown in figure 4(b). Owing to droplet deformation and vaporization, the threshold Reynolds number above which the recirculating eddy forms is considerably lower than that for a hard sphere. The latter case requires a minimum Reynolds number of 20, based on the numerical results of LeClair, Hamielec & Pruppacher (1970) and Dennis & Walker (1971). Figure 4(c) depicts the flow structure with viscous stripping at an ambient velocity of 5 m s^{-1} , showing an oblate droplet with a stretched vortex ring. The flattened edge of the droplet enhances the strength of the recirculating eddies and, as such, dramatically increases the viscous shear stress. Consequently, a thin sheet of fluid is stripped off from the edge of the droplet and swept toward the outer boundary of the recirculating eddy. At a very high ambient velocity of 15 m s^{-1} , droplet fragmentation takes place, as clearly shown in figure 4(d). The hydrogen flow penetrates through the liquid phase, and divides the droplet into two parts: the core disk and the surrounding ring. The vortical structure in the wake region expands substantially as a result of the strong shear stress.

As a result of the difference between mass and thermal diffusivity, the critical mixing state cannot be sustained on the droplet surface after the occurrence of thermodynamic criticality. The surface which attains the critical mixing temperature usually regresses faster than that based on the critical mixing composition. Figure 5 shows the temporal evolution of these two types of critical surfaces under various

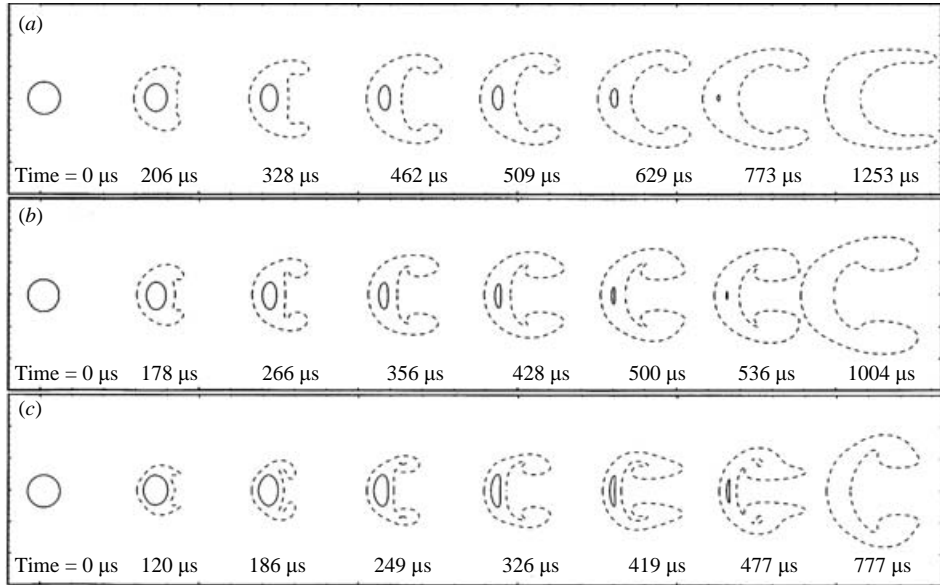


FIGURE 6. Effect of ambient pressure on evolution of droplet critical surfaces, LOX/H₂ system with $U_\infty = 2.5 \text{ m s}^{-1}$ and $D_0 = 100 \mu\text{m}$. (a) $p = 100 \text{ atm}$, (b) 200 atm , (c) 400 atm . —, critical mixing temperature; ---, critical mixing composition.

flow conditions at $p = 100 \text{ atm}$. The initial droplet diameter is $100 \mu\text{m}$. The solid lines represent the instantaneous isotherms of the critical mixing temperature, while the dashed lines mark the surfaces of the critical mixing composition. The values of critical mixing properties can be obtained through a phase-equilibrium analysis (Yang *et al.* 1994) and are given in table 1. Droplet deformation is substantially enhanced by increasing the momentum of the ambient flow. For example, at half of the droplet lifetime, the droplet aspect ratio based on the surface of the critical mixing temperature (defined as the ratio of the length in the radial direction to the thickness in the axis of symmetry) increases from 2.1 at $U_\infty = 2.5 \text{ m s}^{-1}$ to 3.2 at $U_\infty = 5 \text{ m s}^{-1}$. The effects of pressure on the evolution of the critical surfaces are illustrated in figure 6. In addition to enhanced droplet deformation, entrainment of vaporized oxygen into the recirculating eddies in the wake region is augmented with increasing pressure. At $p = 400 \text{ atm}$, the iso-composition skirt even exhibits oscillatory motion. The gaseous oxygen entrapped by the recirculating flow tends to move forward and drives the skirt to expand in the cross-stream direction. The convective flow, on the other hand, suppresses this lateral expansion and forces the skirt to bend and stretch downstream. As a result, more oxygen is trapped into the recirculating eddies, leading to another locomotion.

The transient development of the flow field and droplet evolution can be studied by plotting the instantaneous streamline patterns and temperature field. Figure 7 shows the case for an ambient pressure of 100 atm and velocity of 2.5 m s^{-1} , where the reference x -coordinate moves at the mass-averaged droplet velocity. The initial droplet diameter is $50 \mu\text{m}$. In this low-Reynolds-number case ($Re \approx 15$), the incoming flow passes smoothly over the droplet. There is no recirculating zone behind the droplet at any point in its lifetime; only a stagnant point exists in front of the droplet. The situation, however, becomes drastically different when the incoming velocity increases to 20 m s^{-1} ($Re \approx 120$), as shown in figure 8. A recirculating eddy, which continuously

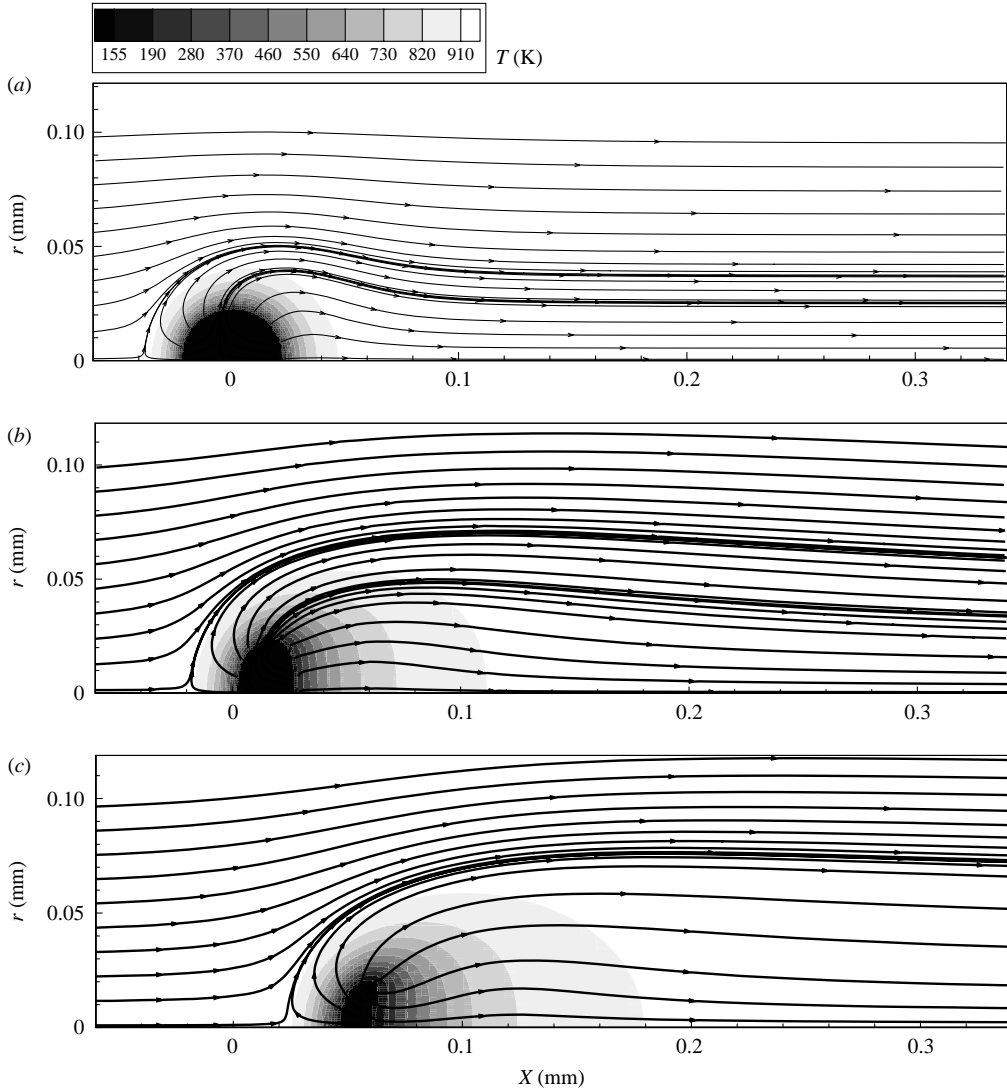


FIGURE 7. Temporal evolution of temperature and flow fields of LOX droplet vaporization in supercritical hydrogen stream; $p = 100$ atm, $U_\infty = 2.5$ m s $^{-1}$, $D_0 = 50$ μ m. (a) $t = 20$ μ s, (b) 200 μ s, (c) 400 μ s.

grows during the vaporization process, appears behind the droplet, and the stagnation point in front of the droplet moves closer to the droplet surface, owing to the stronger aerodynamic force from the incoming hydrogen flow.

Two mechanisms for the formation of a recirculating wake behind a bluff body have been identified (Dandy & Leal 1986; Leal 1989): vorticity accumulation and boundary-layer separation. Leal (1989) pointed out that the recirculating wake behind a bluff body with a smooth slip surface is created by vorticity accumulation. Flow detachment occurs when the dimensionless surface vorticity, defined as $\omega_r = \omega D / U_\infty$ with ω and D being the vorticity and diameter, reaches a critical value of 10.5. This mechanism, however, plays only a minor role in the present study. The vorticity fields presented in figure 9 indicate that the maximum vorticities are far less than 10.5 for all

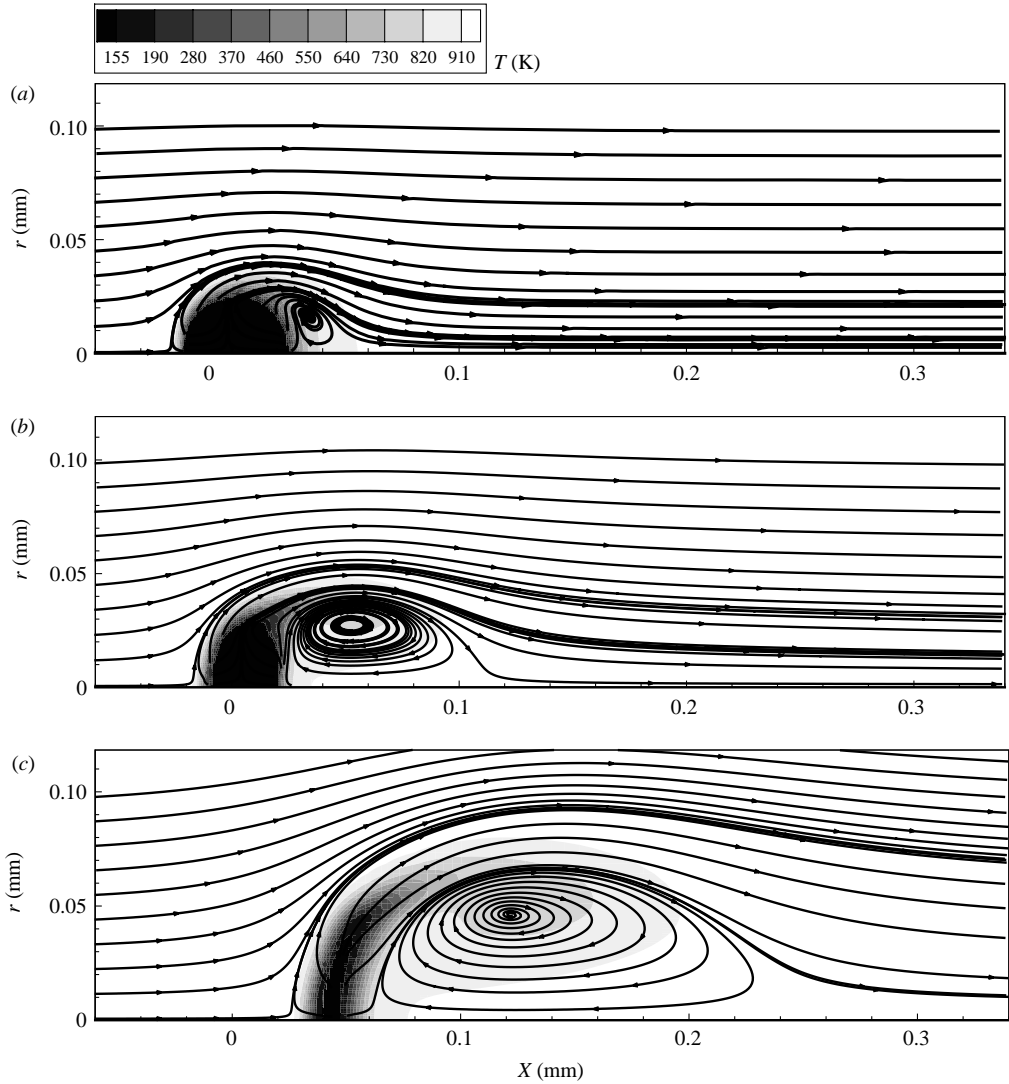


FIGURE 8. Temporal evolution of temperature and flow fields of LOX droplet vaporization in supercritical hydrogen stream; $p = 100$ atm, $U_\infty = 20$ m s $^{-1}$, $D_0 = 50$ μ m. (a) $t = 4$ μ s, (b) 20 μ s, (c) 60 μ s.

the cases considered herein. The formation of a recirculating wake for a supercritical vaporizing droplet is predominantly caused by flow separation, as evidenced by the streamlines in figures 7 and 8. The surface blowing effect resulting from droplet vaporization separates the flow field into the inner and outer regions. A recirculating eddy forms in the inner region when the incoming flow is sufficiently strong. Further stretching of the droplet in the direction perpendicular to the incoming flow enhances flow separation, and facilitates the growth of the recirculating eddy.

Much effort has been applied to the investigation of non-vaporizing droplet deformation and breakup at low pressures (Hinze 1955; Ranger & Nicholls 1969; Wierzbna & Takayama 1988; Pilch & Erdman 1987; Hsiang & Faeth 1992). The process can be characterized with two dimensionless parameters: the Weber and

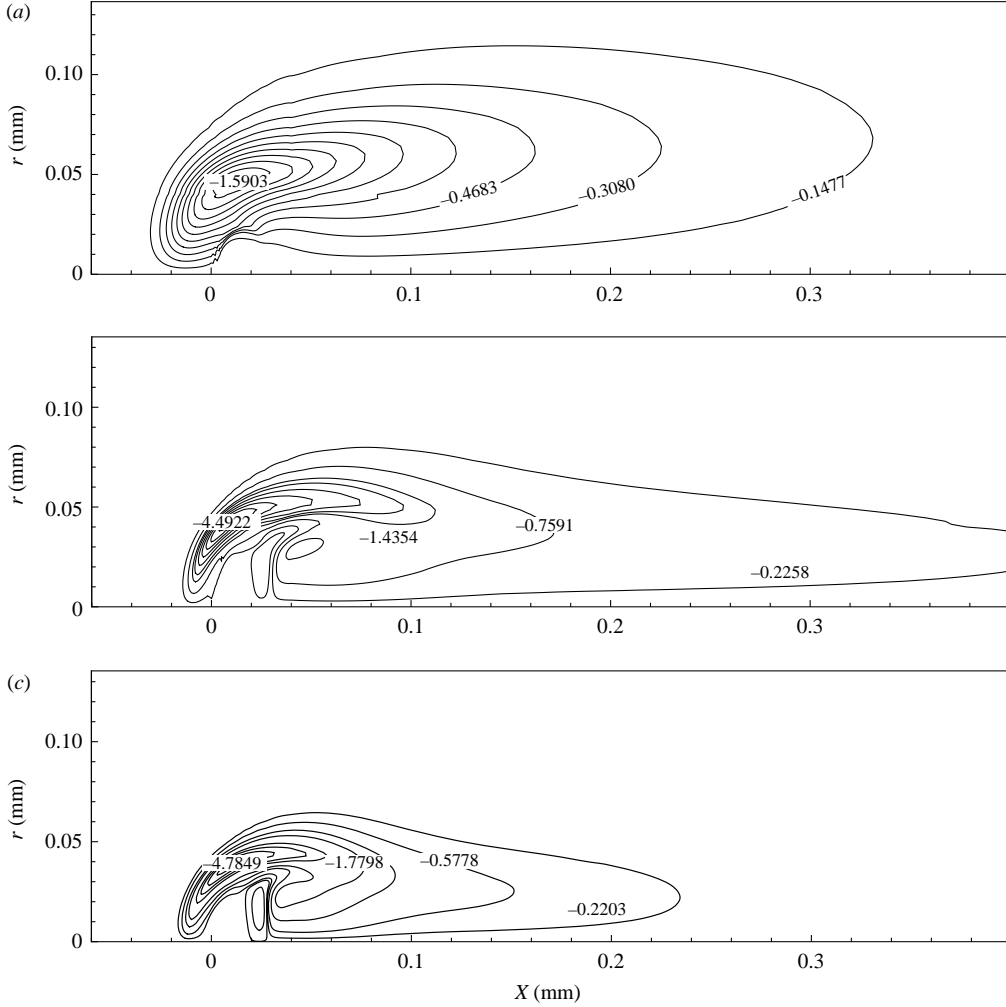


FIGURE 9. Vorticity distributions at different conditions; $D_0 = 50 \mu\text{m}$. (a) $p_\infty = 100 \text{ atm}$, $U_\infty = 2.5 \text{ m s}^{-1}$, $t = 200 \mu\text{s}$; (b) 100, 20, 30; (c) 400, 5, 60.

Ohnesorge numbers. The former, defined as $We = \rho_\infty D_0 U_\infty^2 / \sigma$, represents the ratio of aerodynamic force to surface tension, and the latter, defined as $Oh = \mu_d / \sqrt{\rho_d D_0 \sigma}$, the ratio of viscous force to surface tension. For vaporizing droplets at supercritical conditions, these two numbers approach infinity owing to vanished surface tension. A new dimensionless parameter, denoting the ratio of aerodynamic to viscous forces, is introduced herein to characterize droplet deformation.

$$We^{1/2} / Oh = Re \frac{\mu_\infty}{\mu_d} \sqrt{\frac{\rho_d}{\rho_\infty}}, \quad (5.1)$$

where the subscripts, d and ∞ , represent the properties of the droplet and surrounding fluid, respectively. This parameter is related to the Reynolds number and the ratios of the viscosity and density between the ambient fluid and droplet. It usually decreases with increasing pressure at a given Reynolds number. Table 3 presents some typical values for the oxygen/hydrogen system at three different pressures. As depicted in

Pressures (atm)	Hydrogen at 1000 K		Oxygen at 100 K		$\frac{\mu_\infty}{\mu_d} \sqrt{\frac{\rho_d}{\rho_\infty}}$
	Density ρ_∞ (kg m^{-3})	Viscosity μ_∞ ($10^{-5} \text{ N s m}^{-2}$)	Density ρ_d (kg m^{-3})	Viscosity μ_d ($10^{-4} \text{ N s m}^{-2}$)	
100	2.4	1.968	1118.2	1.721	2.47
200	4.7	1.972	1144.9	1.884	1.63
400	9.0	1.982	1184.3	2.187	1.04

TABLE 3. Thermophysical properties controlling supercritical LOX droplet deformation in hydrogen stream.

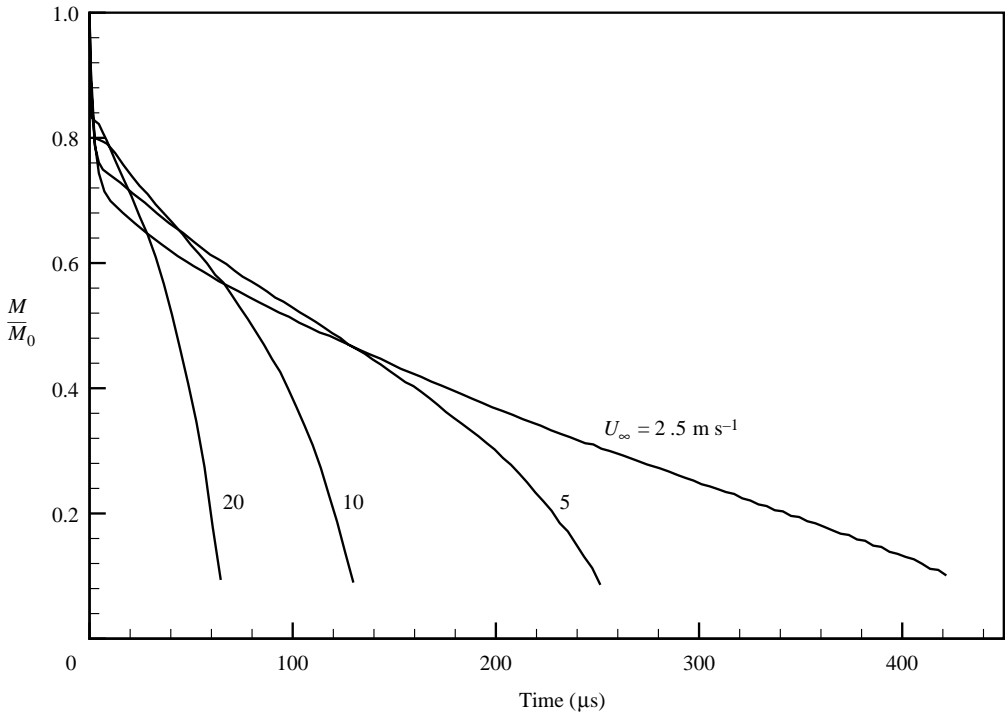


FIGURE 10. Effect of ambient velocity on time evolution of droplet residual mass; LOX/H₂ system with $p = 100$ atm and $D_0 = 50 \mu\text{m}$.

figures 7 and 8 for $D_0 = 50 \mu\text{m}$ (also see figures 2 and 3 for $D_0 = 100 \mu\text{m}$), droplet deformation is enhanced by increasing the Reynolds number at a given pressure. The same observation holds true for cases with the same Reynolds number, but decreasing pressures. For example, the viscous stripping effect disappears when the pressure increases from 100 to 400 atm at a fixed Reynolds number of 120 (Meng 2001). Droplet fragmentation is only observed near the end of the droplet lifetime. At supercritical conditions, it is the combined parameter $We^{1/2}/Oh$ that dominates the droplet dynamics, instead of the individual Weber and Ohnesorge numbers that do not exist.

5.2. Droplet lifetime

An extensive parametric study was conducted to determine the droplet lifetime as a function of ambient flow conditions. Figure 10 presents the effect of ambient velocity on the temporal evolution of droplet residual mass, M , defined herein as

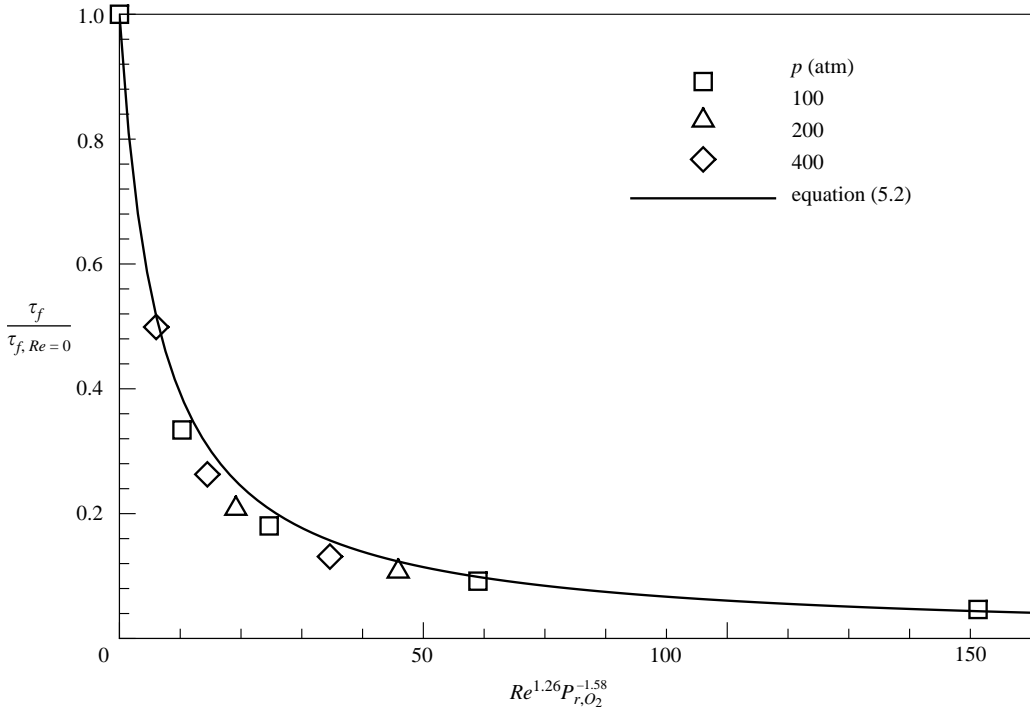


FIGURE 11. Correlation of droplet lifetime as function of free-stream Reynolds number and ambient pressure.

the mass confined by the isothermal surface at the critical mixing temperature, for $p = 100$ atm. The initial droplet diameter D_0 is $50 \mu\text{m}$. In a slowly convective stream, heat conduction plays an important role in determining the vaporization characteristics. The rapid vaporization in the early stage of the droplet lifetime results from the large temperature gradient near the droplet surface. The vaporized oxygen then diffuses outward and hinders the penetration of the thermal wave into the droplet, consequently rendering a slower vaporization rate. At high Reynolds numbers, enhanced heat and mass transfer, along with severe droplet deformation caused by the strong dynamic loading from the approaching flow, considerably facilitates the vaporization process. The droplet disappears within a much shorter period of time. As the pressure increases, the convective heat transfer also increases, since the free-stream Reynolds number varies almost linearly with pressure. In addition, the critical mixing temperature used to define the droplet surface decreases with increasing pressure. These two combined effects apparently favour droplet vaporization at high pressure.

The overall result of droplet lifetime is presented in figure 11, where a simple correlation is developed as

$$\frac{\tau_f}{\tau_{f, Re=0}} = \frac{1}{1 + 0.155 Re^{1.26} (p_{r,O_2})^{-1.58}} \quad (0 < Re < 300, 1 < p_{r,O_2} < 8). \quad (5.2)$$

The Reynolds number, Re , is based on the initial droplet diameter, and p_{r,O_2} is the reduced pressure in reference to the critical pressure of oxygen (i.e. 49.74 atm). The reference time ($\tau_{f, Re=0}$) is chosen to be the lifetime of an isolated droplet vaporizing in a quiescent environment, which can be obtained from Yang *et al.* (1994) and Lafon (1995). Equation (5.2) can be compared with the classical Ranz–Marshall correlation

(Ranz & Marshall 1952) for droplet vaporization in convective environments, which takes the form

$$\frac{\tau_f}{\tau_{f,Re=0}} = \frac{1}{1 + 0.276Re^{1/2}Pr^{1/3}}. \quad (5.3)$$

The Ranz–Marshall correlation is only applicable to low-pressure conditions, and shows a weaker Reynolds-number dependency.

5.3. Droplet drag coefficient

Because of the lack of a distinct gas/liquid interface at supercritical conditions, droplet motion is best characterized based on the locus of the centre of mass, which can be obtained from the first moment of inertia of the mass confined by the critical mixing-temperature surface in reference to a fixed axis. The motion of a droplet is essentially a result of net momentum transfer to it. Following common practice, the drag coefficient is defined as follows:

$$C_D = \frac{M \frac{dU_{drop}}{dt}}{\frac{1}{2}\rho_\infty(U_\infty - U_{drop})^2 \pi R_c^2} \quad (5.4)$$

where $(U_\infty - U_{drop})$ is the droplet relative velocity, and R_c the radius of the mass-equivalent sphere with a uniform distribution of density at its initial value. The denominator in (5.4) represents the aerodynamic loading. The total drag acting on a droplet includes form, friction and thrust drag, of which form drag is usually found to be the dominant component (Haywood, Nafziger & Renksizbulut 1989). Thrust drag arising from the momentum transfer with the ambient flow due to evaporation is negligibly small.

The drag coefficient of an evaporating droplet is usually smaller than that of a hard sphere at the same Reynolds number (Yuen & Chen 1976). This phenomenon may be attributed to the modification of the flow field and transport properties in the vicinity of the droplet surface. The vaporization process often leads to a thickened boundary layer, thereby reducing shear stress and resultant drag. Several workers (e.g. Renksizbulut & Haywood 1988; Haywood *et al.* 1989; Chiang, Raju & Sirignano 1992) have numerically studied this issue by solving the Navier–Stokes equations for a spherical droplet at low to moderate pressures. No deformation was considered, in order to simplify the analysis. The results lead to the following correlation,

$$C_D = \frac{C_D^0}{(1 + B)^b}, \quad (5.5)$$

where C_D^0 is the reference drag coefficient for a hard sphere (Putnam 1961) and takes the form

$$C_D^0 = \frac{24}{Re} \left[1 + \frac{1}{6} Re^{2/3} \right]. \quad (5.6)$$

The coefficient b has a value of 0.2 in Renksizbulut & Haywood's model (1988) and 0.32 in Chiang *et al.*'s model (1992). The Spalding transfer number defined below is adopted to account for the effect of evaporation on drag coefficient,

$$B = \frac{C_p(T_\infty - T_s)}{\Delta h_v}. \quad (5.7)$$

Apparently, the above correlation becomes invalid in the present study of supercritical droplet vaporization. The enthalpy of vaporization Δh_v diminishes to zero when the

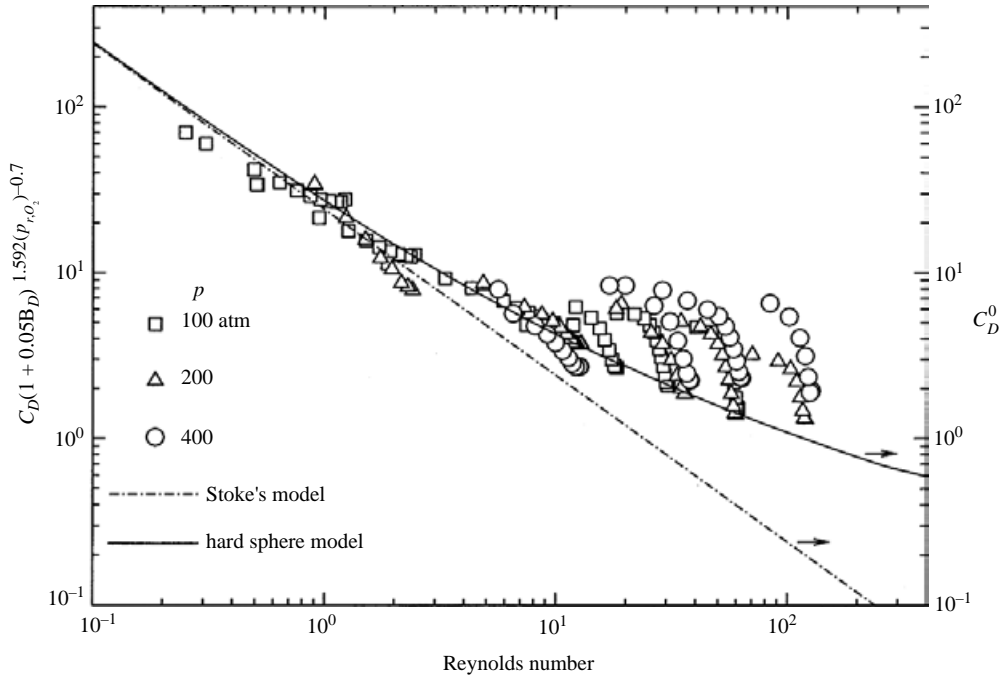


FIGURE 12. Effect of Reynolds number and pressure on droplet drag coefficient.

thermodynamic critical state is reached, rendering a singular value of the transfer number.

To establish a generalized correlation for supercritical conditions, the instantaneous drag force was calculated throughout the entire droplet lifetime for all the scenarios under consideration. The data were then correlated through the use of a transfer number B_D , taking into account the rapid transient during the vaporization process, defined as

$$B_D = \left(\frac{T_\infty - T_c}{T_c - T_l} \right), \quad (5.8)$$

where T_l is the instantaneous average temperature of droplet, and T_c the critical mixing temperature. Since B_D diverges at $T_c = T_l$ at the end of droplet lifetime, the calculation of drag force was terminated when $T_c - T_l$ dropped below 1 K, at which point the droplet residual mass is usually less than one-thousandth of the initial mass. The influence on the accuracy of data reduction is quite limited. Following the procedure leading to (5.5), a correlation shown in figure 12 for LOX droplet drag coefficient is obtained.

$$C_D = \frac{C_D^0}{(1 + aB_D)^b}, \quad (5.9)$$

where a and b are selected to be 0.05 and $1.592(p_{r,O_2})^{-0.7}$, respectively. The data clusters along the classical drag curve, (5.6), in the low-Reynolds-number region, but deviates considerably at high Reynolds numbers (i.e. $Re > 10$). Although a shape factor may be employed to account for this phenomenon, which arises from the increased form drag due to droplet deformation, the difficulty of calculating this factor and conducting the associated data analysis precludes its use in correlating the

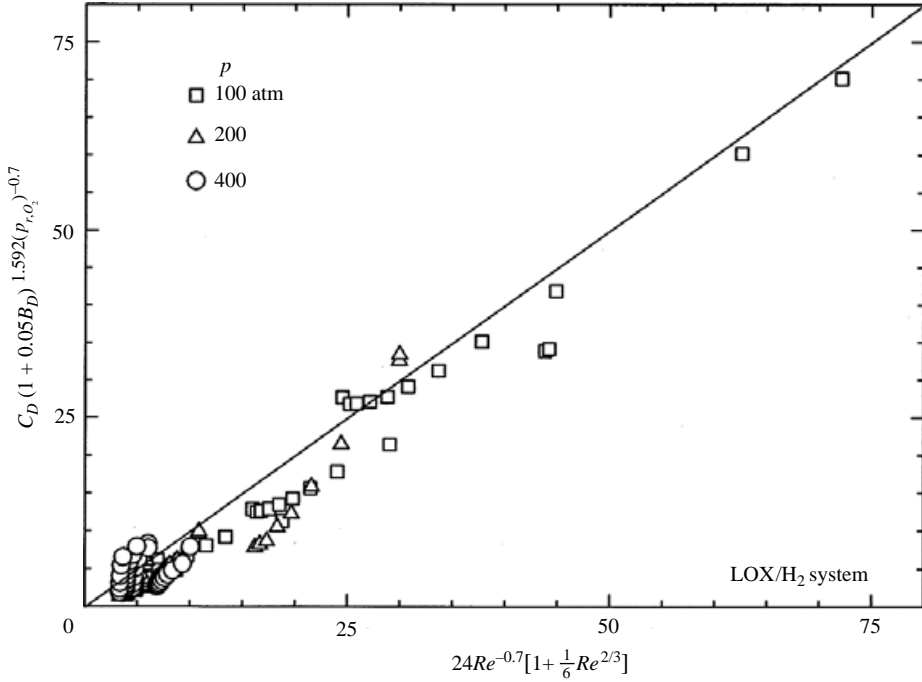


FIGURE 13. Correlation of droplet drag coefficient.

drag coefficient herein. Instead, a simple correction factor $Re^{0.3}$ is incorporated into (5.9) to provide the compensation. The final result shown in figure 13 is

$$C_D = \frac{C_D^0 Re^{0.3}}{(1 + aB_D)^{1.592(p_{r,O_2})^{-0.7}}} \quad (0 < Re < 300, 1 < p_{r,O_2} < 8). \quad (5.10)$$

For a given ambient flow condition, the above correlation requires the transfer function B_D to determine the drag coefficient, which may become cumbersome in practical analyses of spray field dynamics. For convenience, a correlation in terms of the instantaneous droplet mass, instead of the transfer function B_D , is established to bypass this difficulty (Meng 2001)

$$C_D = \frac{A}{Re^{0.24} p_{r,O_2}^{1.164}} \left[\frac{M}{M_0} \right]^{1/3} \quad (0 < Re < 300, 1 < p_{r,O_2} < 8), \quad (5.11)$$

where the coefficient A is

$$A = 71 \frac{\rho_\infty \mu_d^2}{\rho_d \mu_\infty^2}. \quad (5.12)$$

Equation (5.11) indicates that the drag coefficient always decreases with time ($\sim [M/M_0]^{1/3}$) in supercritical droplet vaporization. This differs from that of low-pressure droplet vaporization without droplet deformation (Chiang *et al.* 1992), in which the drag coefficient could either increase or decrease with time during different stages of the droplet lifetime. It generally increases at the end of the vaporization process as a result of the reduced Reynolds number. In supercritical LOX droplet vaporization, the moving velocity of the droplet is relatively small compared with the

free-stream hydrogen velocity. The reduction of the Reynolds number is not sufficient to increase the drag coefficient.

6. Conclusion

The transport and dynamics of liquid oxygen (LOX) droplets in supercritical hydrogen streams has been numerically analysed. The physical model treats the complete conservation equations in an axisymmetric coordinate system, and accommodates thermodynamic non-idealities and transport anomalies in the transcritical regime. The analysis enables a comprehensive investigation into droplet behaviour over a broad range of fluid thermodynamic states and ambient flow conditions. Various key processes involved in droplet vaporization in supercritical forced-convective environments are identified, including flow structures, droplet dynamics and heat and mass transport phenomena. In addition, a parametric study of droplet mass and momentum transfer as a function of ambient pressure (100–400 atm) and Reynolds number (0–300) is conducted. The resultant analytical correlations of droplet lifetime and drag coefficient can be used effectively as a physical submodel in analyses of high-pressure spray field dynamics.

This work was sponsored in part by the US NASA Marshall Space Flight Center and in part by the US Air Force Office of Scientific Research. The support and encouragement of Dr Charles F. Schafer, Mr Marvin Rocker, and Dr Mitat A. Birkan were greatly appreciated.

REFERENCES

- BELLAN, J. 2000 Supercritical (and subcritical) fluid behavior and modeling: drops, streams, shear and mixing layers, jets, and sprays. *Prog. Energy Combust. Sci.* **26**, 329–366.
- CHIANG, C. H., RAJU, M. S. & SIRIGNANO, W. A. 1992 Numerical analysis of convecting, vaporizing fuel droplets with variable properties. *Intl J. Heat Mass Transfer* **35**, 1307–1324.
- CHOI, Y. H. & MERKLE, C. L. 1993 The application of preconditioning in viscous flows. *J. Comput. Phys.* **105**, 207–223.
- DANDY, D. S. & LEAL, L. G. 1986 Boundary-layer separation from a smooth slip surface. *Phys. Fluids* **29**, 1360–1366.
- DAOU, J. & ROGG, B. 1998 Convective burning of gaseous fuel pockets and supercritical droplets. *Combust. Flame* **115**, 145–157.
- DELPLANQUE, J. P. & SIRIGNANO, W. A. 1993 Numerical study of the transient vaporization of an oxygen droplet at sub- and super-critical conditions. *Intl J. Heat Mass Transfer* **36**, 303–314.
- DENNIS, S. C. R. & WALKER, J. D. A. 1971 Calculation of the steady flow past a sphere at low and moderate reynolds numbers. *J. Fluid Mech.* **48**, 771–789.
- ELY, J. F. 1981 An Enskog correction for size and mass difference effects in mixture viscosity prediction. *J. Res. Natl Bureau of Standards* **86**, 597–604.
- ELY, J. F. & HANLEY, H. J. 1981 Prediction of transport properties. 1. Viscosity of fluids and mixtures. *Indust. Engng Chem. Fundamentals* **20**, 323–332.
- ELY, J. F. & HANLEY, H. J. 1983 Prediction of transport properties. 2. Thermal conductivity of pure fluids and mixtures. *Indust. Engng Chem. Fundamentals* **22**, 90–97.
- GRABOSKI, M. S. & DAUBERT, T. E. 1978a A modified Soave equation of state for phase equilibrium calculation. 1. Hydrocarbon systems. *Indust. Engng Chem. Process Design Develop.* **17**, 443–448.
- GRABOSKI, M. S. & DAUBERT, T. E. 1978b A modified Soave equation of state for phase equilibrium calculation. 2. Systems containing CO₂, H₂S, N₂, and CO. *Indust. Engng Chem. Process Design Develop.* **17**, 448–454.

- GRABOSKI, M. S. & DAUBERT, T. E. 1979 A modified Soave equation of state for phase equilibrium calculations. 3. Systems containing hydrogen. *Indust. Engng Chem. Process Design Develop.* **18**, 300–305.
- HARSTAD, K. & BELLAN, J. 1998 Isolated fluid oxygen drop behavior in fluid hydrogen at rocket chamber pressures. *Intl J. Heat Mass Transfer* **41**, 3537–3550.
- HAYWOOD, R. J., NAFZIGER, R. & RENKSIZBULUT, M. 1989 A detailed examination of gas and liquid phase transient processes in convective droplet evaporation. *J. Heat Transfer* **111**, 495–502.
- HINZE, J. O. 1955 Fundamentals of the hydrodynamic mechanism of splitting in dispersion processes. *AIChE J.* **1**, 289–295.
- HSIANG, L. P. & FAETH, G. M. 1992 Near-limit drop deformation and secondary breakup. *Intl J. Multiphase Flow* **18**, 635–652.
- HSIEH, K. C., SHUEN, J. S. & YANG, V. 1991 Droplet vaporization in high-pressure environments. I: Near-critical conditions. *Combust. Sci. Technol.* **76**, 111–132.
- HSIEH, S. Y. & YANG, V. 1997 A preconditioning flux-difference scheme for chemically reacting flows at all mach numbers. *Intl J. Comput. Fluid Dyn.* **8**, 31–49.
- LAFON, P. 1995 Modélisation et Simulation Numérique de L'Evaporation et de la Combustion de Gouttes à Haute Pression. PhD thesis, Université Orléans.
- LEAL, L. G. 1989 Vorticity transport and wake structure for bluff bodies at finite Reynolds numbers. *Phys. Fluids A* **1**, 124–131.
- LECLAIR, B. P., HAMIELEC, A. E. & PRUPPACHER, H. R. 1970 A numerical study of the drag on a sphere at low and intermediate Reynolds numbers. *J. Atmos. Sci.* **27**, 308–315.
- LEVELT SENGERS, J. M. H. 1991 Thermodynamics of solutions near the solvent's critical point. In *Supercritical Fluid Technology* (ed. T. J. Bruno & J. F. Ely) p. 25. CRC Press, Boca Raton, Florida.
- MENG, H. 2001 Liquid-fueled droplet vaporization and cluster behavior at supercritical conditions. PhD dissertation, The Pennsylvania State University, University Park, PA.
- MENG, H. & YANG, V. 2003 A unified treatment of general fluid thermodynamics and its application to a preconditioning scheme. *J. Comput. Phys.* **189**, 277–304.
- PILCH, M. & ERDMAN, C. A. 1987 Use of breakup time data and velocity history data to predict the maximum size of stable fragments for acceleration-induced breakup of a liquid drop. *Intl J. Multiphase Flow* **13**, 741–757.
- PRAKASH, S. & SIRIGNANO, W. A. 1978 Liquid fuel droplet heating and internal circulation. *Intl J. Heat Mass Transfer* **21**, 885–895.
- PRAKASH, S. & SIRIGNANO, W. A. 1980 Theory of convective droplet vaporization with unsteady heat transfer in the circulating liquid phase. *Intl J. Heat Mass Transfer* **23**, 253–268.
- PUTNAM, A. 1961 Integratable form of droplet drag coefficient. *ARS J.* **31**, 1467–1468.
- RANGER, A. A. & NICHOLLS, J. A. 1969 Aerodynamic shattering of liquid drops. *AIAA J.* **7**, 285–290.
- RANZ, W. E. & MARSHALL, W. R. 1952 Evaporation from drops I and II. *Chem. Engng Prog.* **48**, 141–146.
- REID, R. C. PRAUSNITZ, J. M. & POLING, B. E. 1987 *The Properties of Gases and Liquids*, 4th edn. McGraw-Hill.
- RENKSIZBULUT, M. & HAYWOOD, R. J. 1988 Transient droplet evaporation with variable properties and internal circulation at intermediate Reynolds numbers. *Intl J. Multiphase Flow* **14**, 189–202.
- SHUEN, J. S., CHEN, K. H. & CHOI, Y. 1993 A coupled implicit method for chemical non-equilibrium flows at all speeds. *J. Comput. Phys.* **106**, 306–318.
- SHUEN, J. S., YANG, V. & HSHIAO, G. C. 1992 Combustion of liquid-fuel droplets in supercritical conditions. *Combust. Flame* **89**, 299–319.
- TAKAHASHI, S. 1974 Preparation of a generalized chart for the diffusion coefficients of gases at high pressures. *J. Chem. Engng (Japan)* **7**, 417–420.
- VESOVIC, V. & WAKEHAM, W. A. 1991 Transport properties of supercritical fluids and fluid mixtures. *Supercritical Fluid Technology*, edited by Bruno, T. J. and Ely, J. F., CRC Press, Boca Raton, Florida, p. 253.
- WIERZBA, A. & TAKAYAMA, K. 1988 Experimental investigation of the aerodynamic breakup of liquid drops. *AIAA J.* **26**, 1329–1335.

- YANG, V. 2000 Modeling of supercritical vaporization, mixing, and combustion processes in liquid-fueled propulsion systems. *Proc. Combust. Inst.* **28**, 925–942.
- YANG, V., LIN, N. N. & SHUEN, J. S. 1994 Vaporization of liquid oxygen (LOX) droplets in supercritical hydrogen environments. *Combust. Sci. Technol.* **97**, 247–270.
- YUEN, M. C. & CHEN, L. W. 1976 On drag of evaporating liquid droplets. *Combust. Sci. Technol.* **14**, 147–154.
- ZONG, N., MENG, H., HSIEH, S.-Y. & YANG, V. 2004 A numerical study of cryogenic fluid injection and mixing under supercritical conditions. *Phys. Fluids* **16**, 4248–4261.